INTERNATIONAL JOURNAL FOR NUMERICAL METHODS IN FLUIDS
Int. J. Numer. Meth. Fluids **28**: 201–213 (1998)

FREE-SURFACE FLOW OVER CURVED SURFACES PART II: COMPUTATIONAL MODEL

R.C. BERGER[a] AND G.F. CAREY[b,*]

[a] *USAE Waterways Exp. Station, Vicksburg, MS, USA*
[b] *University of Texas, Austin, TX, USA*

SUMMARY

In Part I a detailed derivation of a more general shallow water equation set was developed via a perturbation analysis. A finite element computational model of these more general equations is now constructed and the model behavior is compared with conventional shallow water formulations applied to an outletworks flume. © 1998 John Wiley & Sons, Ltd.

KEY WORDS: curved surface; shallow water; non-hydrostatic; spillway; finite element

1. INTRODUCTION

The momentum equations derived in Part I are in non-conservative form and are written for a specific distance above the bed to include effects due to curvature. The standard two-dimensional shallow water equation formulation assumes a mild bed slope and no curvature effect. These assumptions limit the applicability of these equations for some important classes of problems. In particular, flow over a spillway is indeed affected by the bed curvature via a decidedly non-hydrostatic pressure distribution. In Part II these equations are depth-integrated and incorporated in a computational model. This form of the equations may be useful in handling non-smooth conditions. The weak form solution for the no-curvature condition that would be encountered downstream of the spillway can be made to properly conserve momentum and mass through a hydraulic jump, whereas other forms of the equations may not. In the case in which there is bed curvature, these equations will contain additional terms due to the bed curvature which, while finite through the jump, will make an additional contribution that can cause an error in the jump location. Therefore, in the vicinity of the jump these equations, which properly conserve mass and momentum for the no-curvature case, will conserve mass precisely in the curved bed state only. Generally, in practical cases the strong jump is restricted to the region downstream of the spillway face where the bed contains no curvature.

Several recent finite element schemes for the shallow water equations utilize the Petrov–Galerkin approach [1,2] and are considered in Reference [3]. Such a scheme is constructed here for the system developed in Part I to handle bed curvature effects. The treatment proceeds as follows: first the model equations are summarized and an appropriate test function is devised. Next, the finite element Petrov–Galerkin system is presented and the treatment of boundary

* Correspondence to: USAE Waterways Exp. Station, Vicksburg, MS, USA.

CCC 0271–2091/98/120201–13$17.50
© 1998 John Wiley & Sons, Ltd.
Received December 1996
Revised April 1997

conditions, viscous stresses, bottom friction model etc. is discussed. Some flume comparison studies conclude the work.

2. MODEL EQUATIONS AND FINITE ELEMENT TREATMENT

From Part I, the equations for the curved bed formulation are

$$\mathbf{L}(\mathbf{Q}) = \mathbf{M}_t + \frac{1}{\zeta_1\zeta_2}\left[\frac{\partial(\zeta_2\mathbf{N}_a)}{\partial s_1} + \frac{\partial(\zeta_1\mathbf{N}_b)}{\partial s_2}\right] + \frac{1}{\zeta_1\zeta_2}\mathbf{H} = 0, \tag{1}$$

where

$$\mathbf{Q}^T = [h \;\; p \;\; q], \qquad p = \hat{u}h, \qquad q = \hat{v}h, \quad \text{and} \quad f_1(s_3) = 1 - \kappa_1 s_3, \qquad f_2(s_3) = 1 - \kappa_2 s_3, \tag{2}$$

with

$$\mathbf{M} = \begin{Bmatrix} f_1(h)f_2(h)h \\ f_2\left(\frac{h}{2}\right)p \\ f_1\left(\frac{h}{2}\right)q \end{Bmatrix},$$

$$\mathbf{N}_a = \begin{Bmatrix} pc_1 \\ \frac{p^2}{h^2}a_2 + \frac{1}{2}\frac{p^2}{h^2}\left[\frac{a_1}{(f_1(h))^2} - a_2\right] + \frac{1}{2}\frac{q^2}{h^2}\left[\frac{a_1}{(f_2(h))^2} - a_3\right] + g_3[ha_1 - a_4] \\ \frac{pq}{h^2}b_3 \end{Bmatrix},$$

$$\mathbf{N}_b = \begin{Bmatrix} qc^2 \\ \frac{pq}{h^2}a_3 \\ \frac{q^2}{h^2}b_2 + \frac{1}{2}\frac{q^2}{h^2}\left[\frac{b_1}{(f_2(h))^2} - b_2\right] + \frac{1}{2}\frac{p^2}{h^2}\left[\frac{b_1}{(f_1(h))^2} - b_3\right] + g_3[hb_1 - b_4] \end{Bmatrix}.$$

In the non-homogeneous term $H^T = [H_1 \; H_2 \; H_3]$ with

$$H_1 = 0,$$

$$H_2 = \frac{1}{2}\frac{p^2}{h^2}\left\{-\frac{\partial\zeta_2}{\partial s_1}\left[\frac{a_1}{(f_1(h))^2} - a_2\right] + \zeta_2\frac{\partial\kappa_2}{\partial s_1}\left[\frac{1}{2}\left(\frac{h}{f_1(h)}\right)^2 - a_5\right]\right\}$$
$$+ \frac{1}{2}\frac{q^2}{h^2}\left\{-\frac{\partial\zeta_2}{\partial s_1}\left[\frac{a_1}{(f_2(h))^2} - a_3\right] + \zeta_2\frac{\partial\kappa_2}{\partial s_1}\left[\frac{1}{2}\left(\frac{h}{f_2(h)}\right)^2 - a_6\right]\right\}$$

© 1998 John Wiley & Sons, Ltd.

$$+\frac{q^2}{h^2}\left[-\frac{\partial\zeta_2}{\partial s_1}a_3+\zeta_2\frac{\partial\kappa_2}{\partial s_1}a_6\right]+\frac{pq}{h^2}\left[\frac{\partial\zeta_1}{\partial s_2}a_3-\zeta_1\frac{\partial\kappa_1}{\partial s_2}a_8\right]$$
$$+\kappa_1\frac{p}{h}\left\{\left[\frac{\partial}{\partial s_1}\left(\frac{\zeta_2 p}{h}\right)\right]a_9-\frac{\zeta_2 p}{h}\frac{\partial\kappa_2}{\partial s_1}a_{10}+2\zeta_2\frac{p}{h}\frac{\partial\kappa_1}{\partial s_1}a_{11}+\frac{\partial}{\partial s_2}\left(\frac{\zeta_1 q}{h}\right)a_{12}-\frac{\zeta_1 q}{h}\frac{\partial\kappa_1}{\partial s_2}a_{13}\right.$$
$$\left.+2\frac{\zeta_1 q}{h}\frac{\partial\kappa_2}{\partial s_2}a_{14}\right\}+g_3\left\{-\frac{\partial\zeta_2}{\partial s_1}[ha_1-a_4]+\frac{\zeta_2 h^3}{6}\frac{\partial\kappa_2}{\partial s_1}\right\}+\zeta_1\zeta_2 g_1 a_7,$$

$$H_3=\frac{1}{2}\frac{q^2}{h^2}\left\{-\frac{\partial\zeta_1}{\partial s_2}\left[\frac{b_1}{(f_2(h))^2}-b_2\right]+\zeta_1\frac{\partial\kappa_1}{\partial s_1}\left[\frac{1}{2}\left(\frac{h}{f_2(h)}\right)^2-b_5\right]\right\}$$
$$+\frac{1}{2}\frac{p^2}{h^2}\left\{-\frac{\partial\zeta_1}{\partial s_2}\left[\frac{b_1}{(f_1(h))^2}-b_3\right]+\zeta_1\frac{\partial\kappa_1}{\partial s_2}\left[\frac{1}{2}\left(\frac{h}{f_1(h)}\right)^2-b_6\right]\right\}$$

$$+\frac{p^2}{h^2}\left[-\frac{\partial\zeta_1}{\partial s_2}b_3+\zeta_1\frac{\partial\kappa_1}{\partial s_2}b_6\right]+\frac{pq}{h^2}\left[\frac{\partial\zeta_2}{\partial s_1}b_3-\zeta_2\frac{\partial\kappa_2}{\partial s_1}b_8\right]$$
$$+\kappa_2\frac{q}{h}\left\{\left[\frac{\partial}{\partial s_2}\left(\frac{\zeta_1 q}{h}\right)\right]b_9-\frac{\zeta_1 q}{h}\frac{\partial\kappa_1}{\partial s_2}b_{10}+2\zeta_1\frac{q}{h}\frac{\partial\kappa_2}{\partial s_2}b_{11}+\frac{\partial}{\partial s_1}\left(\frac{\zeta_2 p}{h}\right)b_{12}-\frac{\zeta_2 p}{h}\frac{\partial\kappa_2}{\partial s_1}b_{13}\right.$$
$$\left.+2\frac{\zeta_2 p}{h}\frac{\partial\kappa_1}{\partial s_1}b_{14}\right\}+g_3\left\{-\frac{\partial\zeta_1}{\partial s_2}[hb_1-b_4]+\frac{\zeta_1 h^3}{6}\frac{\partial\kappa_1}{\partial s_2}\right\}+\zeta_1\zeta_2 g_2 b_7,$$

where the coefficients a_i, b_i and c_i result from depth integration

$$a_1=\int_0^h f_2(s_3)\,\mathrm{d}s_3,\qquad a_2=\int_0^h\frac{f_2(s_3)}{(f_1(s_3))^2}\,\mathrm{d}s_3,\qquad a_3=\int_0^h\frac{1}{f_2(s_3)}\,\mathrm{d}s_3,$$

$$a_4=\int_0^h s_3 f_2(s_3)\,\mathrm{d}s_3,\qquad a_5=\int_0^h\frac{s_3}{(f_1(s_3))^2}\,\mathrm{d}s_3,\qquad a_6=\int_0^h\frac{s_3}{(f_2(s_3))^2}\,\mathrm{d}s_3,$$

$$a_7=\int_0^h f_1(s_3)f_2(s_3)\,\mathrm{d}s_3,\qquad a_8=\int_0^h\frac{s_3}{f_1(s_3)f_2(s_3)}\,\mathrm{d}s_3,$$

$$a_9=\int_0^h\frac{1}{(f_1(s_3))^2}\int_0^{s_3}\frac{f_2(\xi)}{f_1(\xi)}\,\mathrm{d}\xi\;\mathrm{d}s_3,\qquad a_{10}=\int_0^h\frac{1}{(f_1(s_3))^2}\int_0^{s_3}\frac{\xi}{f_1(\xi)}\,\mathrm{d}\xi\;\mathrm{d}s_3,$$

$$a_{11}=\int_0^h\frac{1}{(f_1(s_3))^2}\int_0^{s_3}\frac{\xi f_2(\xi)}{(f_1(\xi))^2}\,\mathrm{d}\xi\;\mathrm{d}s_3,\qquad a_{12}=\int_0^h\frac{1}{(f_1(s_3))^2}\int_0^{s_3}\frac{f_1(\xi)}{f_2(\xi)}\,\mathrm{d}\xi\;\mathrm{d}s_3,$$

$$a_{13}=\int_0^h\frac{1}{(f_1(s_3))^2}\int_0^{s_3}\frac{\xi}{f_2(\xi)}\,\mathrm{d}\xi\;\mathrm{d}s_3,\qquad a_{14}=\int_0^h\frac{1}{(f_1(s_3))^2}\int_0^{s_3}\frac{\xi f_1(\xi)}{(f_2(\xi))^2}\,\mathrm{d}\xi\;\mathrm{d}s_3,$$

$$c_1=\frac{1}{\kappa_1 h}\left[\left(\frac{\kappa_2-\kappa_1}{\kappa_1}\right)\log f_1(h)+\kappa_2 h\right],\qquad c_2=\frac{1}{\kappa_2 h}\left[\left(\frac{\kappa_1-\kappa_2}{\kappa_2}\right)\log f_2(h)+\kappa_1 h\right].$$

The coefficients b_i are simply obtained by exchanging the subscripts 1 and 2 in the right-hand-sides of these equations for a_i.

© 1998 John Wiley & Sons, Ltd.

The Petrov–Galerkin formulation incorporates a combination of the Galerkin test function and a non-Galerkin component to control oscillations due to convection. It is sufficient to consider the zero-curvature case only when selecting the test functions. This is significantly simpler than including curvature and can be justified on physical grounds. The shallow water equations (with ζ_1 and ζ_2 not identically equal to 1) then simplify to

$$\frac{\partial \mathbf{Q}}{\partial t} + \mathbf{A}\frac{\partial \mathbf{Q}}{\partial s_1} + \mathbf{B}\frac{\partial \mathbf{Q}}{\partial s_2} = \mathbf{H}, \tag{3}$$

where $\mathbf{Q}$ and $\mathbf{H}$ have the same form as before and now

$$\mathbf{A} = \frac{1}{\zeta_1}\begin{bmatrix} 0 & 1 & 0 \\ (c^2 - u^2) & 2u & 0 \\ -uv & v & u \end{bmatrix},$$

$$\mathbf{B} = \frac{1}{\zeta_2}\begin{bmatrix} 0 & 0 & 1 \\ -uv & v & u \\ (c^2 - v^2) & 0 & 2v \end{bmatrix},$$

where $c = (g_3 h)^{1/2}$ and g_3 is the gravitational component in the bed-normal direction. Let $\lambda_1 = u/\zeta_1$, $\lambda_2 = (u + c)/\zeta_2$, $\lambda_3 = (u - c)/\zeta_3$ denote the eigenvalues of $\mathbf{A}$, and $\mathbf{P}$ be the 3×3 matrix of right eigenvectors. Similarly, let $\gamma_i = 1, 2, 3$ be the eigenvalues of $\mathbf{B}$, and $\mathbf{R}$ the corresponding matrix. The test function then has the form

$$\boldsymbol{\psi} = \phi \mathbf{I} + \boldsymbol{\varphi}, \tag{4}$$

where

$$\boldsymbol{\varphi} = \epsilon\left(\Delta s_1 \frac{\partial \phi}{\partial s_1}\hat{\mathbf{A}} + \Delta s_2 \frac{\partial \phi}{\partial s_2}\hat{\mathbf{B}}\right). \tag{5}$$

Here $\hat{\mathbf{A}} = \mathbf{P}^{-1}\hat{\mathbf{\Lambda}}\mathbf{P}$ with

$$\hat{\mathbf{\Lambda}} = \begin{bmatrix} \dfrac{\lambda_1}{|\lambda_1|} & 0 & 0 \\ 0 & \dfrac{\lambda_2}{|\lambda_2|} & 0 \\ 0 & 0 & \dfrac{\lambda_3}{|\lambda_3|} \end{bmatrix}, \qquad \mathbf{P} = \begin{bmatrix} -v & 0 & 1 \\ -\zeta_1\lambda_3 & 1 & 0 \\ -\zeta_1\lambda_2 & 1 & 0 \end{bmatrix},$$

$$\mathbf{P}^{-1} = \frac{1}{2c}\begin{bmatrix} 0 & 1 & -1 \\ 0 & \zeta_1\lambda_2 & -\zeta_1\lambda_3 \\ 2c & v & -v \end{bmatrix}, \tag{6}$$

and

$$\hat{\mathbf{B}} = \mathbf{R}^{-1}\hat{\mathbf{\Gamma}}\mathbf{R}, \tag{7}$$

© 1998 John Wiley & Sons, Ltd.

with

$$\hat{\mathbf{\Gamma}} = \begin{bmatrix} \dfrac{\gamma_1}{|\gamma_1|} & 0 & 0 \\ 0 & \dfrac{\gamma_2}{|\gamma_2|} & 0 \\ 0 & 0 & \dfrac{\gamma_3}{|\gamma_3|} \end{bmatrix}, \qquad \mathbf{R} = \begin{bmatrix} -u & 1 & 0 \\ -\zeta_2\gamma_3 & 0 & 1 \\ -\zeta_2\gamma_2 & 0 & 1 \end{bmatrix},$$

$$\mathbf{R}^{-1} = \frac{1}{2c} \begin{bmatrix} 0 & 1 & -1 \\ 2c & u & -u \\ 0 & \zeta_2\gamma_2 & -\zeta_2\gamma_3 \end{bmatrix}. \tag{8}$$

The test function in Equation (4) will now be used in a Petrov–Galerkin finite element formulation for the model equations (1) including bed curvature.

The weighted residual statement becomes

$$\int_\Omega \left(\phi \mathbf{M}_t - \frac{1}{\zeta_1}\frac{\partial \phi}{\partial s_1}\mathbf{N}_a - \frac{1}{\zeta_2}\frac{\partial \phi}{\partial s_2}\mathbf{N}_b + \frac{\phi}{\zeta_1\zeta_2}\mathbf{H} + \boldsymbol{\varphi}\mathbf{L} \right) \mathrm{d}\Omega + \oint_{\partial\Omega} \phi(\mathbf{N}_a n_1 + \mathbf{N}_b n_2)\,\mathrm{d}l = 0, \tag{9}$$

where, n_1 and n_2 are the components of the outward normal vector to the boundary.

A slip flow boundary at a solid wall corresponds to the condition $u_n = 0$ and is imposed through the weak statement for mass conservation and momentum conservation in directions s_1 and s_2

$$\int_{\partial\Omega} \phi(pc_1 n_1 + qc_2 n_2)\,\mathrm{d}l = 0, \tag{10}$$

$$\int_{\partial\Omega} \phi\left(\frac{p^2}{h^2}a_2 n_1 + \frac{pq}{h^2}a_3 n_2\right)\mathrm{d}l = 0, \tag{11}$$

$$\int_{\partial\Omega} \phi\left(\frac{pq}{h^2}b_3 n_1 + \frac{q^2}{h^2}b_2 n_2\right)\mathrm{d}l = 0. \tag{12}$$

The upstream boundary condition is an essential condition. If the flow here is subcritical then the flow components are specified as either $\hat{u}$ and $\hat{v}$ or p and q. If the flow is supercritical the depth is also specified. The downstream boundary condition is unspecified if the flow is supercritical there. If the flow is subcritical the depth is specified by substituting the specified depth in the boundary integral terms of the momentum equations.

The viscous stress is of less importance in the calculation of the free-surface, except as the flow passes through the hydraulic jump. The contribution is small when the flow is smooth. The present stress calculation is based upon the velocity and metric gradients at the bed, so that a lateral or longitudinal stress is not produced by the assumed vertical velocity profile. The stresses [4] then are

$$\sigma_{11} = 2\nu\rho\left(\frac{1}{\zeta_1}\frac{\partial \hat{u}}{\partial s_1} + \frac{\hat{v}}{\zeta_1\zeta_2}\frac{\partial \zeta_1}{\partial s_2}\right), \tag{13}$$

$$\sigma_{21},\ \sigma_{12} = \nu\rho\left(\frac{1}{\zeta_2}\frac{\partial \hat{u}}{\partial s_2} + \frac{1}{\zeta_1}\frac{\partial \hat{v}}{\partial s_1} - \frac{\hat{v}}{\zeta_1\zeta_2}\frac{\partial \zeta_2}{\partial s_1} - \frac{\hat{u}}{\zeta_1\zeta_2}\frac{\partial \zeta_1}{\partial s_2}\right), \tag{14}$$

© 1998 John Wiley & Sons, Ltd.

$$\sigma_{22} = 2\nu\rho\left(\frac{1}{\zeta_2}\frac{\partial \hat{v}}{\partial s_2} + \frac{\hat{u}}{\zeta_1\zeta_2}\frac{\partial \zeta_2}{\partial s_1}\right). \tag{15}$$

The first subscript indicates the face upon which the stress acts and the second is its direction. When applied to the present numerical system, the following additional contributions to the respective momentum equations are obtained

$$ST_1 = \int_\Omega \frac{a_7}{\rho}\left(\frac{1}{\zeta_1}\frac{\partial \phi}{\partial s_2}\sigma_{11} + \frac{1}{\zeta_2}\frac{\partial \phi}{\partial s_2}\sigma_{21}\right) \mathrm{d}\Omega, \tag{16}$$

$$ST_2 = \int_\Omega \frac{b_7}{\rho}\left(\frac{1}{\zeta_1}\frac{\partial \phi}{\partial s_1}\sigma_{12} + \frac{1}{\zeta_2}\frac{\partial \phi}{\partial s_2}\sigma_{22}\right) \mathrm{d}\Omega. \tag{17}$$

These contributions are included in the left-hand-side of Equation (9). The stress jump across inter-element boundaries is set to zero and a stress-free boundary is assumed along the domain edge.

The turbulent eddy viscosities generated by the bottom friction are given by [5,6]

$$\nu_t = C_B h f^{1/2} |u|, \tag{18}$$

where ν_t is the turbulent viscosity, C_B is a coefficient that varies between 0.1 and 1.0, and f is the Darcy–Weisbach friction coefficient (see e.g. Reference [7]). The turbulent contribution to viscosity is generally much larger than the molecular viscosity.

The common practise in hydraulic engineering of using an empirical relationship developed by Manning and extended to curved beds in one dimension by Dressler and Yevjevich [8] is adopted here. This is extended to two dimensions. Therefore, the force per unit mass as it appears on the right-hand-side of the s_1 momentum equation becomes

$$Fb_1 = -\frac{gn^2 p(p^2+q^2)^{1/2}}{h a_7^{4/3}}, \tag{19}$$

and similarly for the s_2 momentum equation

$$Fb_2 = -\frac{gn^2 q(p^2+q^2)^{1/2}}{h b_7^{4/3}}. \tag{20}$$

These terms are included in Equation (9) for the bed drag force.

The finite element approximation for Equation (9) becomes

$$\sum_e \left[\int_{\Omega_e}\left(\phi_i \tilde{\mathbf{M}}_t - \frac{1}{\tilde{\zeta}_1}\frac{\partial \phi_i}{\partial s_1}\tilde{\mathbf{N}}_a - \frac{1}{\tilde{\zeta}_2}\frac{\partial \phi_i}{\partial s_2}\tilde{\mathbf{N}}_b + \frac{\phi_i}{\tilde{\zeta}_1\tilde{\zeta}_2}\tilde{\mathbf{H}} + \boldsymbol{\varphi}_i\tilde{\mathbf{L}}\right)\mathrm{d}\Omega_e + \oint_{\partial\Omega_e\cap\partial\Omega}\phi_i(\tilde{\mathbf{N}}_a n_1 + \tilde{\mathbf{N}}_b n_2)\,\mathrm{d}l\right] = 0, \tag{21}$$

where the symbol $\sim$ indicates the discrete value of the quantity and the subscript indicates a particular test function. The geometry and flow variables are represented using the finite element basis; e.g.

$$\tilde{\mathbf{Q}} = \sum_j \phi_j \mathbf{Q}_j,$$

and the function $\boldsymbol{\varphi}_i$ is defined as

$$\boldsymbol{\varphi}_i = \epsilon\left(\Delta s_1 \frac{\partial \phi_i}{\partial s_1}\tilde{\tilde{\mathbf{A}}} + \Delta s_2 \frac{\partial \phi_i}{\partial s_2}\tilde{\tilde{\mathbf{B}}}\right).$$

© 1998 John Wiley & Sons, Ltd.

Quadrilateral bilinear elements with nodes at the element corners are used. The grid intervals Δs_1 and Δs_2 in the physical domain are chosen in the same manner as Katopodes [1]

$$\Delta s_1 = 2\left[\left(\frac{\partial s_1}{\partial \xi}\right)^2 + \left(\frac{\partial s_1}{\partial \eta}\right)^2\right]^{1/2}, \qquad \Delta s_2 = 2\left[\left(\frac{\partial s_2}{\partial \xi}\right)^2 + \left(\frac{\partial s_2}{\partial \eta}\right)^2\right]^{1/2}. \tag{22}$$

The temporal derivative may be represented as

$$\gamma \frac{\mathbf{Q}_j^{n+1} - \mathbf{Q}_j^n}{\Delta t} + (1-\gamma)\frac{\mathbf{Q}_j^n - \mathbf{Q}_j^{n-1}}{\Delta t} \doteqdot \frac{\partial \mathbf{Q}_j^{n+1}}{\partial t}, \tag{23}$$

where the subscript j indicates a particular node location and the superscript indicates the time step. If $\gamma = 3/2$, this defines a second-order backward difference in time; if $\gamma = 1$ the standard first-order backward difference is obtained (both schemes are unconditionally stable for the linear problem). Within a time step, Newton Raphson iteration is used to solve the non-linear problem set.

3. OUTLETWORKS FLUME

Previously, one-dimensional tests have demonstrated the importance of the Dressler equations in problems with bed curvature [3,9–12]. The formulation is extended to two-dimensions in Part I and in the present section the validity of a computational representation of these equations on a problem with two-dimensional variation is investigated. The numerical test presented here is of an outletworks flume that is supercritical throughout containing bed curvature and lateral transitions. Model resolution is refined until no significant change results from additional refinement. Additional numerical studies of simpler cases including comparison with data [10–12] are given in Reference [3].

The steep slope, St. Venant and the present generalized model equations are compared with data for an outletworks physical model at the Waterways Experiment Station, WES. Here, our primary concern is the lateral behavior predicted by the mathematical models for realistic structures. A diagram of the flume, as tested, is shown in Figure 1. The plan view geometry for the flume and the model are identical but the numerical approximation to bed elevation has smooth transitions to provide a continuous slope. The dimensions of the flume were chosen such that typical operating conditions place the flow regime within the fully turbulent region. For the present test, the Reynolds number is about $R \equiv uh/v \approx 200\,000$, which indicates that scale effects are small. For even relatively smooth bed and wall conditions the flume will be in the fully turbulent regime (see References [13,14]). Therefore, the flume results can reasonably be expected to exhibit behavior similar to large-scale structures of this type.

The bed elevation of the flume is purposely laid out longitudinally as a parabolic function to minimize flow separation. The actual dimensions in Figure 1 are 'as measured' and vary slightly from the construction specifications, primarily as a result of settling. The transition from the circular conduit to the apron is fairly complicated. The walls have a slight flair with a radius of 2.75 ft and the bed has fillets to move smoothly from the round conduit to the rectangular section of the apron. The apron wall has an outward slope of ≈ 6. A level stilling basin which contains baffles and an end sill is located 4.015 ft from the conduit exit. These stilling basin features are not numerically modeled here because these effects far downstream are of lesser importance to the spillway flow. The actual bed elevation numerically modeled (as shown in Figure 1) contains no discontinuities in slope so that the curvature exists throughout. The bed is flat in the lateral direction, i.e. all slope and curvature variations are in the longitudinal direction.

© 1998 John Wiley & Sons, Ltd.

The flume water surface is recorded every 0.05 ft laterally and every 0.10 ft longitudinally. An additional reading is made near the sidewalls (typically within 0.02 ft). The measurements are recorded with a point gage capable of measuring to a precision of 0.001 ft (it is graduated in 0.01 ft units and with a vernier changes of 0.001 can be detected). In reality the water surface is quite rough and time varying, so that readings are approximately accurate to ≈ 0.02 ft. The flow rate is measured using a 12×6 inch venturi meter with a differential manometer. The inflow pressure is maintained by a constant head tank. The manometer calibration is checked using direct measurements of volume change in a specific time period. The discharge is estimated to be accurate within 3% (C.H. Tate, private communication).

The flume water surface results are shown in Figure 2 as a three-dimensional perspective for a flow rate of 2.56 cfs (cubic feet per second). The view shows the lateral hump in the water surface as the flow exits the outlet conduit. This eventually spreads to a relatively uniform depth as intended in the design. If flow becomes focused, however, the result will be circulation in the stilling basin with possible damage there. The non-uniform velocity field would also

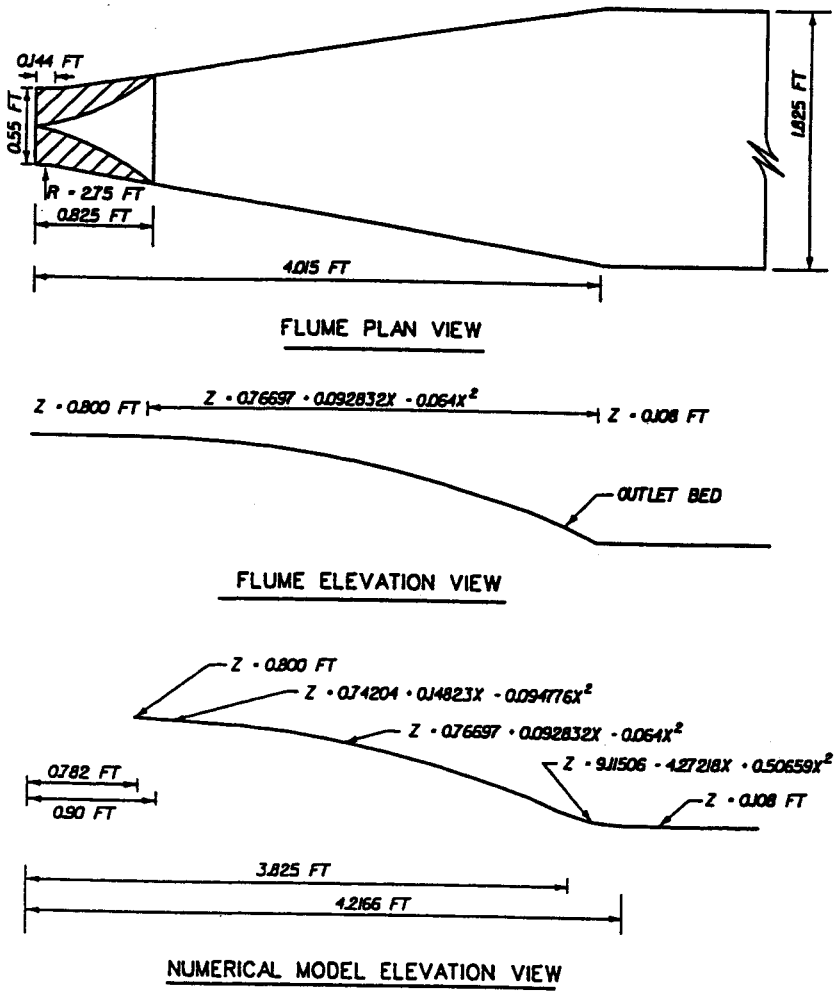

Figure 1. Outletworks flume: flume and numerical model geometry.

© 1998 John Wiley & Sons, Ltd.

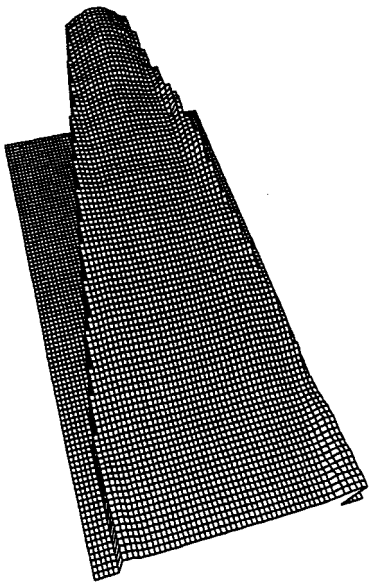

Figure 2. Outletworks flume: water surface results, perspective view.

cause more downstream erosion. The drag of the apron sidewalls causes the sharp rise in water surface. The build-up in water depth along the sides of the stilling basin is a result of the change in side slopes.

The numerical model is constructed of 408 nodes and 368 elements (see Figure 3). It extends longitudinally from $x = 0.75$ to 6.0 ft. The upstream boundary is therefore below the complex geometry of the fillets near the conduit exit and the vertical velocity profile should be closer to an open-channel flow distribution. The flow is supercritical throughout the study reach, and at the upstream boundary the velocity and depths are specified. The depths are the flume results interpolated from the 0.70 and 0.80 ft ranges. The z component velocity distribution is assumed to be uniform across the upstream boundary. The lateral velocity component at the inlet is specified so that the flow is tangent to the sidewalls and zero in the channel center with

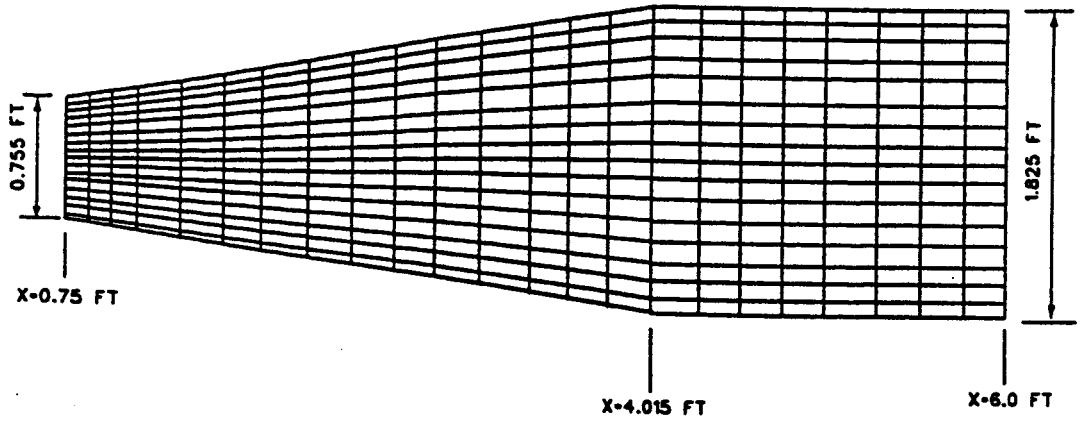

Figure 3. Outletworks model: computational mesh.

© 1998 John Wiley & Sons, Ltd.

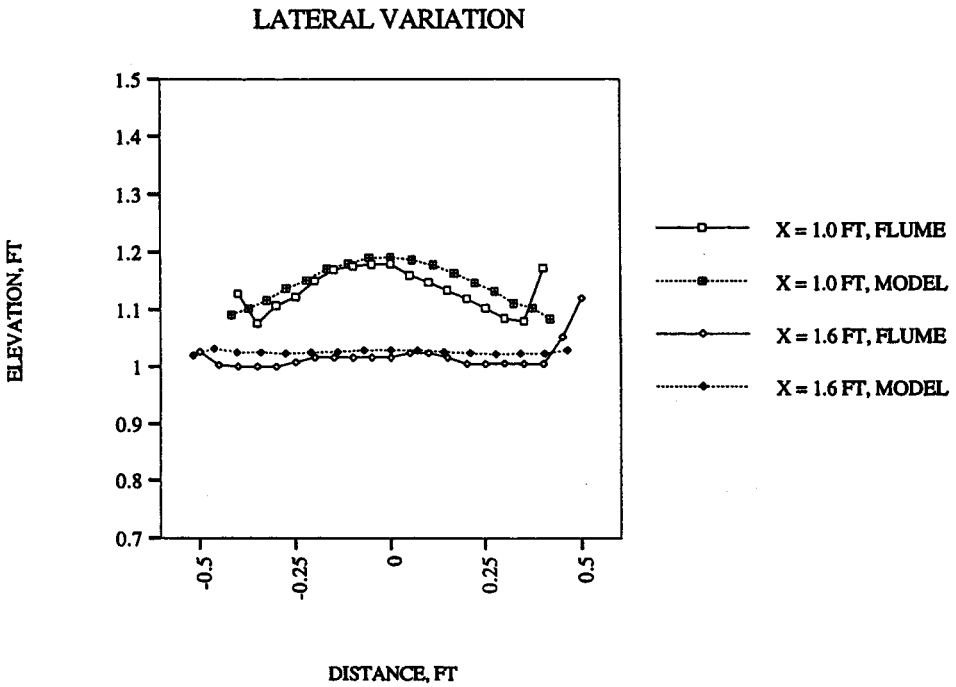

Figure 4. Water surface results showing model and flume comparison at sections $x = 1.0$ and 1.6 ft.

linear variation between these stations. These are the simplest reasonable boundary conditions and should be suitable for a comparison of model equations. Furthermore, this is as much information as a modeler usually has in order to make a site-specific study. The turbulent viscosity $\nu_t = 0.05$ f^2 s^{-1} corresponds to a value of $C_B \approx 0.1$. Other parameter values for the calculation are: $m = 0.012$, $\Delta t = 0.05$ s, $\epsilon = 0.03$ and $g = 32.208$ f s^{-2}. The simulation time is 15 s and a maximum of 3 N iterations per step is required. Figure 4 shows the water surface elevation at sections $x = 1.0$ and 1.6 ft for flume results and the generalized shallow water equation model. Both show the rapid collapse of the flow plume along the channel length. A direct comparison shows the standard deviation of the difference between the flume and model to be 0.032 and 0.022 ft at $x = 1.0$ and 1.6 ft, respectively. The model plume drops to a more uniform water surface elevation somewhat more quickly than the flume.

More detail is found in Figures 5–8 which show the depth contours for the flume, the generalized shallow water equations, the standard steep-slope shallow water equations, and the St. Venant equations. The flume and St. Venant measurements are made vertically as water surface elevations which we have converted to depths normal to the bed. The flume data in the upper region reveals a continuation of the conduit shape, i.e. a hump in the water surface with the centerline being a relative maximum. This form ends near $x = 1.75$ ft. From there on, the centerline is a relative minimum or the surface is nearly flat. This is the desired pattern for a good hydraulic design. At the channel edges the wall drag causes a substantial build-up of water depth.

A most important result of the generalized shallow water equations is the more gradual lateral spread of the flow tube. As an illustration, within the portion of the flume modeled here, the flume shows the centerline to be a relative maximum for about 1.0 ft. The model

© 1998 John Wiley & Sons, Ltd.

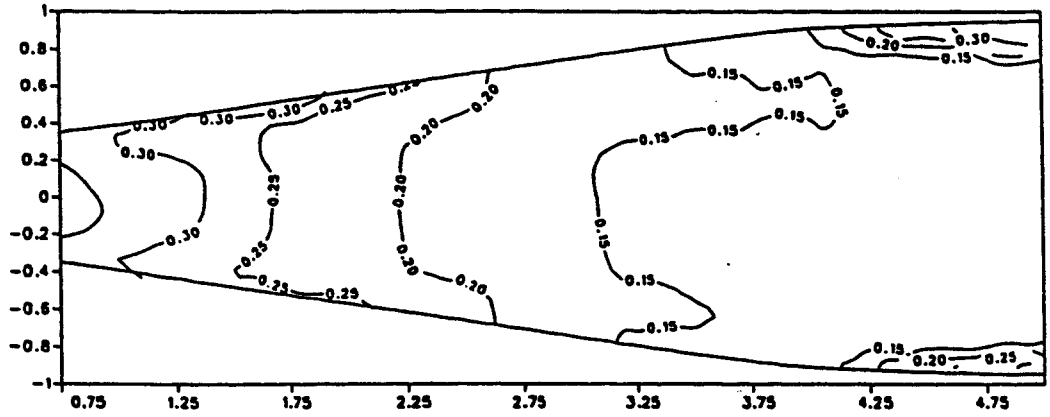

Figure 5. Outletworks flume: depth contours.

including curvature gave a similar length. The steep-slope shallow water model (no curvature) and the St. Venant equations are nearly identical throughout the domain. The length for which the centerline is a maximum as predicted by these models is only ≈ 0.7 ft. Hence, the non-hydrostatic component has a definite effect upon the wave speed here. The lateral variation is strongly dependent upon the non-hydrostatic contribution. The predicted wave celerity for a similar case in which the curvature and dominant flow direction are along the x-axis can be shown [9] to be

$$c_{gswe} = \left\{ -\frac{\log(1-\kappa_1 h)}{(1-\kappa_1 h)\kappa_1}\left[g_3 + \frac{\kappa_1 \hat{u}^2}{(1-\kappa_1 h)^3}\right]\right\}^{1/2}. \tag{24}$$

On the other hand, the celerity without curvature included is simply

$$c_{sswe} = (g_3 h)^{1/2}. \tag{25}$$

A convex curvature (κ_1 negative) produces a lower celerity in the generalized equations which is not captured in the standard shallow water equations. The true solution, which includes non-hydrostatic pressure contributions as a result of short wavelengths in addition to bed

Figure 6. Outletworks model: generalized shallow water equations, depth contours.

© 1998 John Wiley & Sons, Ltd.

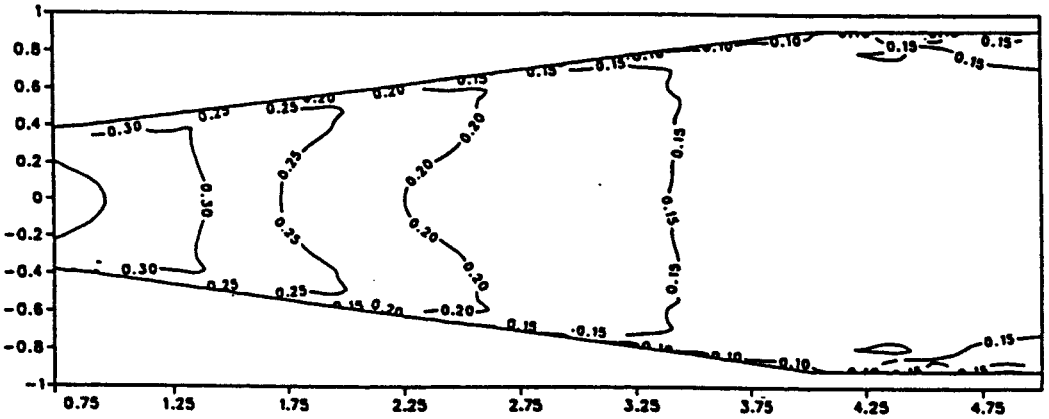

Figure 7. Outletworks model: standard steep-slope shallow water equations, depth contours.

curvature effects, has a wave celerity that is even smaller than the generalized equations predict. In a concave region (positive curvature) the wave celerity predicted by the generalized shallow water equations will be greater than that predicted by the standard shallow water equations.

4. CONCLUSION

A generalized shallow water equation set to reproduce free-surface flow over curved beds has been developed in this investigation and the model has been applied to spillway flows. These generalized shallow water equations include bed curvature effects, and are non-hydrostatic and two-dimensional. The equations are derived via a perturbation expansion in a shallowness parameter. A significant assumption made in this derivation is that the flow is irrotational about axes parallel to the plane of the bed. However, there is no limitation on vorticity about axes normal to the bed.

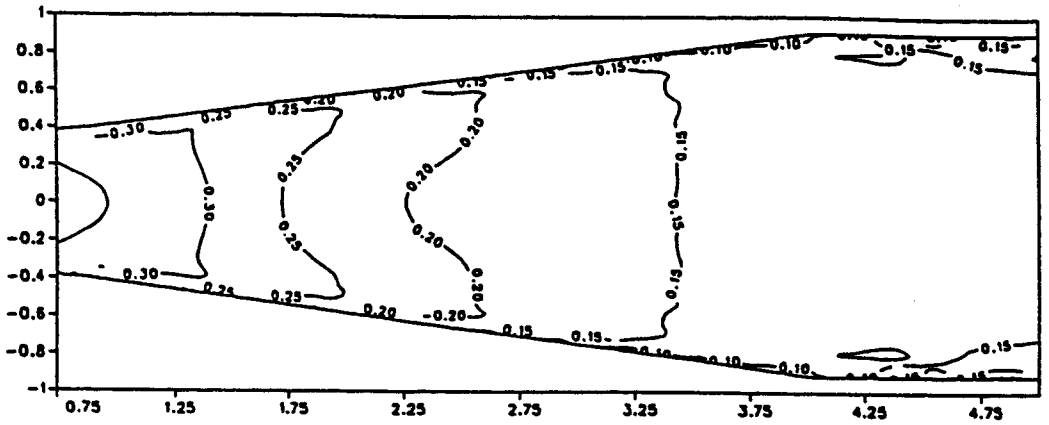

Figure 8. Outletworks model: St. Venant equations, depth contours.

© 1998 John Wiley & Sons, Ltd.

The final development involved a two-dimensional model in which the non-linear terms were addressed via a Newton Raphson technique, iterating at each time step. A Petrov–Galerkin scheme was introduced, based on the SUPG idea in which the test function is weighted using the eigenvalues of the convection matrices.

One-dimensional tests reported elsewhere [3] for a curved bottom flume with straight walls compared remarkably well with the flume water surface data. The spillway capacity was accurately captured and a comparison of bed pressure was quite good. The St. Venant and the standard steep-slope shallow water equations missed the spillway capacity, both prediciting a greater water surface elevation to attain the steady discharge. (The hydrostatic pressure assumption misses the reduction in pressure caused by the uplift of the flow over the curved crest. This is responsible for the error in spillway capacity.) Along the downstream face the standard steep-slope formulation compared quite well with the generalized shallow water equations and flume data. The St. Venant equations predicted too steep a water surface slope. This was shown to be a result of the mild-slope assumption, and was not curvature related. The principal improvement of the new equations over the 'no-curvature case' is in the neighborhood of the spillway crest.

In the present work, experimental data on a flume at the Waterways Experiment Station was collected to study outlet works. Here the emphasis was upon lateral variations in water surface. The improvement offered by the new equations was subtle showing slower (and more realistic) spread of the flow conduit over negative curvature regions. Overall, however, the representation of what is essentially a short wave phenomena was weak. However, the results did provide a qualitative picture of the flow that is beneficial for designers.

ACKNOWLEDGMENTS

This investigation has been supported in part by the US Army Waterways Experiment Station and by ARPA.

REFERENCES

1. N.D. Katopodes, 'Two-dimensional surges and shocks in open channels', *ASCE J. Hydraul. Eng.*, **110**, 794–812 (1984).
2. R.C. Berger and R.L. Stockstill, 'Finite-element model for high-velocity channels', *ASCE J. Hydraul. Eng.*, **121**, 710–716 (1995).
3. R.C. Berger, 'Free-surface flow over curved surfaces', *Ph.D. dissertation*, Dept. of Engrg. Mech., University of Texas at Austin, TX, 1992.
4. A.P. Boresi and K.P. Chong, *Elasticity in Engineering Mechanics*, Elsevier Science, New York, 1987, p. 220.
5. W. Rodi, 'Turbulence models and their application in hydraulics—A state of the art review', State-of-the-Art Paper, *International Association for Hydraulic Research*, Delft, Netherlands, 1980.
6. R.S. Chapman and C.Y. Kuo, 'Application of the two-equation k–ϵ turbulence model to a two-dimensional, steady, free surface flow problem with separation', *Int. j. numer. methods fluids*, **5**, 257–268 (1985).
7. H.W. King and E.F. Grater, *Handbook of Hydraulics for the Solution of Hydrostatic and Fluid-Flow Problems*, McGraw-Hill, New York, 1963.
8. R.F. Dressler and V. Yevjevich, 'Hydraulic-resistance terms modified for the Dressler curved-flow equations', *J. Hydraul. Res.*, **22**, 145–156 (1984).
9. R.F. Dressler, 'New nonlinear shallow-flow equations with curvature', *J. Hydraul. Res.*, **16**, 205–222 (1978).
10. N.S. Sivakumaran, 'Shallow-flow over curved beds', *Doctoral Dissertation*, Asian Institute of Technology, Bangkok, Thailand, 1981.
11. N.S. Sivakumaran, R.J. Hosking, T. Tingsanchali, 'Steady shallow flow over a spillway', *J. Fluid Mech.*, **111**, 411–420 (1981).
12. N.S. Sivakumaran, T. Tingsanchali and R.J. Hosking, 'Steady shallow flow over curved beds', *J. Fluid Mech.*, **128**, 469–487 (1983).
13. A.J. Reynolds, *Turbulent Flows in Engineering*, Wiley, London, 1974, p. 196–230.
14. V.T. Chow, *Open-Channel Hydraulics*, McGraw-Hill, New York, 1959.

© 1998 John Wiley & Sons, Ltd.